Dynamics of droplet formation and flow regime transition in a T-shaped microfluidic device with a shear-thinning continuous phase

Venu Gopal Agarwal, Rattandeep Singh, Supreet Singh Bahga, and Amit Gupta*
Department of Mechanical Engineering, Indian Institute of Technology Delhi, New Delhi, Delhi 110016, India

(Received 30 August 2019; accepted 31 March 2020; published 28 April 2020)

A numerical and experimental study of the process of droplet formation in a T-junction microchannel with a shear-thinning continuous phase is presented. Simulations are performed using a three-dimensional lattice Boltzmann multicomponent model. The shear-thinning behavior is modeled using the Carreau-Yasuda model and validated with our experiments involving both Newtonian and non-Newtonian continuous phases. Using the validated numerical framework, a parametric study is performed to quantify the effect of the rheological parameters, namely, the power-law index n and the Carreau number Cr, on the droplet size for two different capillary numbers. To understand the variation in the droplet size and shape with the shear-thinning parameters, the dynamics of the droplet breakup process is analyzed in terms of the upstream pressure buildup and the shear stresses acting on the interface of the two fluids. Our numerical results show that the dynamics of droplet formation shifts from the shear-dominated dripping regime to the pressure-dominated squeezing regime for continuous phase fluids having lower values of n and higher values of Cr. Hence, an increase in the droplet size and a change in its shape from spherical to plug are observed for fluids showing a higher shear-thinning tendency (higher Cr and lower n). Finally, an analysis of the transition in the droplet flow regimes with a shear-thinning continuous phase at high capillary numbers is presented. For Ca $\geqslant 0.1$, an increase in the shear thinning of the continuous fluid is shown to shift the droplet flow pattern from parallel flow to droplets in the channel to eventually forming droplets at the T junction.

DOI: 10.1103/PhysRevFluids.5.044203

I. INTRODUCTION

Droplet-based microfluidic technology involves generation and manipulation of discrete droplets using immiscible fluids inside microdevices [1–4]. Independent control of these microdroplets has enabled their widespread application in the synthesis of nanomaterial [5,6], drug delivery [7,8], food processing [9,10], and medical diagnostics [11,12]. Microdroplets have been used as compartments for carrying out biological and chemical reactions, thus serving as individual units for reactions [13,14]. These microreactors help in significantly reducing reaction time by enhancing mixing and mass transfer rates. Multiple such microreactors have been used to carry out massive parallel processing and experimentation, which has led to high-throughput chemical and biological analysis [15]. The majority of these applications require droplets to be generated in a controlled and uniform manner. Therefore, it is essential to have a thorough understanding of the phenomenon of droplet generation to have precise control over their size and frequency in these microfluidic devices.

In droplet flows, the characteristics of the droplet produced, such as their size, shape, and uniformity, depend upon the physical mechanism of their generation. Generally, three different

*agupta@mech.iitd.ac.in

regimes of droplet formation have been identified: squeezing [16,17], dripping, and jetting [18–20]. The occurrence of a particular formation regime is determined by the geometrical design of the microchannel, viscosities, flow rates, and interfacial tension of the two fluids. The microchannel geometries used for generating droplets can be classified into coflow [18–20], flow-focusing [21–23], and crossflow [24–41] categories. The T-junction microfluidic device is a commonly used crossflow geometry for droplet generation in which the dispersed and the continuous phase flowing through two orthogonal channels interact at the T junction, forming droplets in the process. The dimensionless parameters influencing the size and formation regime of the droplets generated at the T junction include capillary number Ca, flow rate ratio, viscosity ratio, width, and aspect ratio of the channel.

At very low values of capillary number ($\mathrm{Ca} < 10^{-2}$), droplet formation takes place in the squeezing regime [27]. Droplets formed in this regime are in the form of long plugs, the length of which has been shown to depend predominantly on the flow rate ratio [27] and the channel confinement (width and aspect ratio) [35]. The effect of the capillary number and the viscosity ratio is negligible in the squeezing regime [29]. For higher values of capillary number ($\mathrm{Ca} > 10^{-2}$), the dripping regime of droplet formation is prevalent, in which the droplet size is much smaller compared to the squeezing regime [29]. The dynamics of droplet breakup in this regime is controlled predominantly by shear stresses exerted by the continuous phase on the interface of the dispersed phase. The droplet size follows an inversely proportional power-law relationship with the capillary number [28,31]. Within the dripping regime, on increasing the capillary number (roughly $\mathrm{Ca} > 10^{-1}$), the breaking point of the droplets is sent further downstream of the T junction, leading to droplet formation in the channel (DC) [29]. With a further increase in the capillary number, the DC regime finally transforms into a stable parallel flow [25]. Apart from the capillary number, previous experimental and numerical studies have shown that the flow regime transition from dripping to parallel flow also depends on the viscosity ratio and geometric parameters of the channel [25,32,36].

The transition from the low-capillary-number squeezing regime to the high-capillary-number dripping regime is gradual and is marked by an intermediate or transition regime ($\mathrm{Ca} \sim 10^{-2}$) in which both the viscous shear stress and squeezing pressure influence the breakup dynamics of the droplet [30,34,42,43]. The droplets formed in this regime are in the form of truncated disks, the size of which was observed to depend on both the flow rate ratio and capillary number [26,30,31] as well as on geometric parameters and viscosity ratio [36]. Another regime of droplet formation, known as the leaking regime [44], has been discovered recently that manifests for a capillary number lower than that for the squeezing regime. It has been observed that for such negligibly small values of Ca, the dependence of Ca on droplet size is reintroduced.

The process of droplet generation in a microfluidic T junction for Newtonian fluids has been thoroughly analyzed in the literature. Compared to Newtonian systems, droplet generation involving non-Newtonian fluids has been poorly understood owing to the complex nonlinear rheological behavior and associated elastic effects. A thorough understanding of such a system would enable the application of microdroplets to biology and pharmaceuticals where the fluids involved are mainly non-Newtonian in nature (physiological fluids such as blood). The special character associated with the non-Newtonian fluids in the form of shear-dependent viscosity and viscoelasticity has shown to significantly influence the dynamics of the droplet formation process, consequently affecting the size of the droplet generated in flow-focusing [45–49], coflowing [50], or T-junction geometries [51–61]. In a T-junction geometry, the Newtonian droplet generation in a shear-thinning inelastic continuous fluid has been identified as a particular subset of problems concerning droplet generation in non-Newtonian systems. A few numerical [57,58] and experimental studies [59–61] addressing this problem have shown that the shear-thinning property of the continuous fluid has a considerable impact on the droplet size. However, an exhaustive description of the droplet breakup mechanism and the transition in the droplet formation regime with a shear-thinning continuous phase is still lacking and demands further investigation.

In this study, the process of droplet formation in a T-junction microchannel with a shear-thinning continuous phase is investigated numerically and experimentally. A three-dimensional

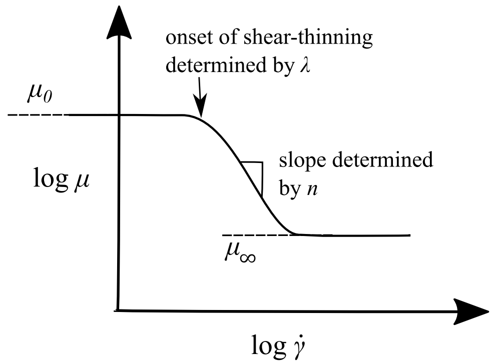

FIG. 1. Schematic of the Carreau-Yasuda shear-thinning model.

multicomponent model based on the multiple-relaxation-time lattice Boltzmann method is employed to simulate the droplet formation phenomenon in a T-junction microchannel for a shear-thinning continuous phase. The numerical model is validated by comparing the simulations with our experimental observations of droplet formation in a Newtonian as well as a shear-thinning continuous phase. A numerical parametric study is then performed to quantitatively analyze the effect of rheological parameters such as the power-law index and the Carreau number on the droplet size for a range of capillary numbers. To understand the variation in the droplet size and shape with the shear-thinning parameters, the dynamics of the droplet breakup process is analyzed in terms of upstream pressure buildup and the shear stress acting on the dispersed phase. Finally, a transition in the droplet flow regimes is shown at high capillary numbers due to the shear-thinning behavior of the continuous phase. In this study the dynamics of the droplet formation and its transition for a Carreau-Yasuda (CY) [62] shear-thinning continuous phase is analyzed.

II. DESCRIPTION OF THE SYSTEM

A. Carreau-Yasuda shear-thinning fluids

The most common approach to modeling the shear-thinning behavior of a non-Newtonian fluid is to adopt a basic power-law equation. However, such a model unrealistically predicts very high viscosities (approaching infinity) at very low values of shear rate. The Carreau-Yasuda model [62], on the other hand, is a more practical rheological approach since it is able to predict the Newtonian plateau (constant viscosities) at either extreme of shear rates, an observation consistent with experimental rheological data for viscous shear-thinning solutions [62]. The general form of the CY model is given by

$$\mu(\vec{x},t) = \mu_\infty + (\mu_0 - \mu_\infty)[1 + (\lambda|\dot{\gamma}|^\beta)]^{(n-1)/\beta}. \tag{1}$$

Here μ is the shear-dependent dynamic viscosity, μ_∞ and μ_0 are the dynamic viscosities at infinite and zero-shear rates, respectively, n is the power-law index, λ is the inelastic time constant, $|\dot{\gamma}|$ is the second invariant of the strain rate tensor, and β is a parameter controlling the curvature of the curve at the transition from the zero-shear-rate Newtonian region to the power-law region. The schematic representation of the CY model is shown in Fig. 1. In the present study, a simplified form of generalized CY model [63] is used. It is a three-parameter model obtained by substituting $\beta = 2$ and $\mu_\infty = 0$ in Eq. (1) and is expressed as

$$\mu(\vec{x},t) = \mu_0[1 + (\lambda|\dot{\gamma}|^2)]^{(n-1)/2}. \tag{2}$$

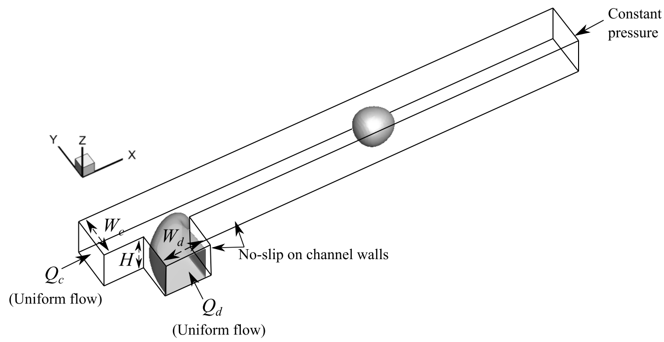

FIG. 2. Schematic of the T-junction microchannel used for simulating the phenomenon of droplet formation.

B. Problem formulation

Figure 2 shows a schematic of the computational domain used for simulating the phenomenon of droplet formation in a T-junction microchannel. The geometry of the T junction, as shown in Fig. 2, consists of two orthogonal inlets and a common outlet. The continuous or the carrier phase fluid flows in the main channel, while the dispersed phase fluid is supplied by the orthogonal channel. The inlet channels for the continuous and the dispersed phase are rectangular in cross section with widths W_c and W_d, respectively, and with the same depth H. A uniform velocity profile is imposed at the channel inlets by specifying the equilibrium distribution functions $f_{i,\text{inlet}}^{\text{eq}}(\rho, \vec{u}_{\text{inlet}})$ at every time step [36]. Similarly, $f_{i,\text{outlet}}^{\text{eq}}(\rho_{\text{outlet}}, \vec{u})$ is used for the constant pressure boundary condition at the outlet. A no-slip boundary condition is applied at the walls of the channels using a halfway bounceback scheme [36]. The interfacial interaction between the fluids and the solid walls is specified such that the continuous phase wets the walls of the main channel while the dispersed phase is completely nonwetting.

The process of droplet formation at a T junction can be affected by a variety of parameters such as the height and the width of the inlet channels, inlet flow rates of the dispersed and the continuous phase (Q_c and Q_d), and the material properties of the two fluids which include their viscosities, densities, and the interfacial tension between them (σ). For multicomponent flows in microfluidic systems, the buoyancy force being a volume force is much smaller than surface forces. Therefore, for the sake of simplicity, the two fluids are assumed to be of equal density ρ [29]. The viscosity of the shear-thinning continuous phase fluid is characterized in terms of three independent rheological parameters (as described earlier), which are the zero-shear viscosity $\mu_{c,0}$, the inelastic time constant λ, and the power-law index n.

Using the Buckingham-π theorem, the dimensional parameters affecting the size of a Newtonian droplet in a shear-thinning continuous phase fluid are nondimensionalized to give a set of eight independent dimensionless parameters as given in Eq. (3), which have been used to characterize the droplet size

$$\bar{V} = f\,(\Gamma, \Lambda, \Phi, Q, \text{Re}, \text{Ca}, \text{Cr}, n). \tag{3}$$

Here $\Gamma = H/W_c$ and $\Lambda = W_d/W_c$ are the aspect ratio and the width ratio of the channels, respectively, while $\Phi = \mu_d/\mu_{c,0}$ and $Q = Q_c/Q_d$ are the viscosity and the flow rate ratio of the two fluids, respectively; $\text{Re} = \rho Q_c/H\mu_{c,0}$ is the Reynolds number, $\text{Ca} = \mu_{c,0}Q_c/HW_c\sigma$ is the capillary number, and $\text{Cr} = \lambda Q_c/H^2W_c$ is the Carreau number. The droplet size is quantified in terms of the nondimensional droplet volume as $\bar{V} = V_{\text{droplet}}/W_c^3$. The Carreau number is representative of the onset of shear-thinning behavior and is inversely proportional to the critical shear rate at which the transition from Newtonian to power-law behavior occurs. The power-law index n, on the other hand, is representative of the sensitivity of the viscosity to changes in the shear rate. For fluids with either Cr $\ll 1$ or $n = 1$, the shear stress becomes linearly proportional to the strain rate, i.e., the Newtonian behavior is completely restored with $\mu = \mu_{c,0}$.

III. NUMERICAL METHODOLOGY

A multicomponent model based on the lattice Boltzmann method (LBM) is employed for simulating the droplet formation process in a shear-thinning continuous phase. A multiple-relaxation-time version of the color-gradient multicomponent model is implemented. The LBM is particularly advantageous in simulating non-Newtonian fluid flows [64] since the strain rate tensor which is used for determining the shear-dependent viscosity can be calculated locally at each and every lattice site, thereby eliminating the necessity of using a differencing scheme for velocity gradient calculations as is required in the case of Navier-Stokes solvers. Additionally, the second-order accuracy of the LBM is retained for shear-thinning flows, and the parallel implementation of the LBM solver is made much easier as the shear rates are computed locally.

A. Lattice Boltzmann equation

The fundamental variable in the LBM is the discrete velocity distribution function, the evolution (both spatial and temporal) of which is governed by the lattice Boltzmann equation (LBE), given by

$$f_i(\vec{x} + \vec{e}_i \Delta t, t + \Delta t) = f_i(\vec{x}, t) + \Omega_i(\vec{x}, t) + F_i(\vec{x}, t). \tag{4}$$

Here $f_i(\vec{x}, t)$ denotes the distribution function which is defined at points $\vec{x}$ located on a cubic lattice with lattice spacing Δx and at time step Δt. Additionally, the distribution function f_i is defined for a discrete set of directions i along which the particle populations move with speed given by $\vec{e}_i$. Further, $\Omega_i(\vec{x}, t)$ is the collision operator and $F_i(\vec{x}, t)$ is the source term due to the external force on the fluid. The macroscopic mass density ρ and momentum density $\rho\vec{u}$ are obtained by taking moments of the distribution function as given by, respectively,

$$\rho(\vec{x}, t) = \sum_i f_i(\vec{x}, t), \tag{5}$$

$$\rho\vec{u}(\vec{x}, t) = \sum_i f_i(\vec{x}, t)\vec{e}_i + \frac{\vec{F}(\vec{x}, t)\Delta t}{2}, \tag{6}$$

where the external forces have been accounted for by using a second-order scheme [65] and f_i^{eq} is the local equilibrium function given by

$$f_i^{\mathrm{eq}} = \rho w_i \left[1 + \frac{\vec{e}_i \cdot \vec{u}}{c_s^2} + \frac{(\vec{e}_i \cdot \vec{u})^2}{2c_s^4} - \frac{\vec{u} \cdot \vec{u}}{2c_s^2} \right], \tag{7}$$

with w_i the weight coefficient associated with each discrete velocity vector. In the nearly incompressible limit, the LBE can be reduced to the Navier-Stokes equation (NSE) with second-order accuracy by using the Chapman-Enskog expansion along with Eqs. (5) and (6) [66]. As a consequence of this link between the LBE and NSE, the pressure p and dynamic shear viscosity μ can be expressed as

$$\mu = \rho c_s^2 \left(\tau - \frac{\Delta t}{2} \right), \tag{8}$$

$$p = \rho c_s^2, \tag{9}$$

where τ is the relaxation time and c_s is the speed of sound (assuming isothermal conditions), which is given by

$$c_s^2 = \frac{1}{3} \left(\frac{\Delta x}{\Delta t} \right)^2. \tag{10}$$

B. Multiple-relaxation-time model

The multiple-relaxation-time (MRT) formulation [67] is used to model the particle collisions. Since the fluids simulated in the present study exhibit strong rheological properties (widely varying viscosities), the MRT formulation has been extended to enhance the numerical stability of the fluid solver [68]. The MRT collision operator Ω_i used in the LBE (4) is given by

$$\Omega_i(\vec{x},t) = -(\mathbf{M}^{-1}\mathbf{S}\mathbf{M})_{ij}[f_j(\vec{x},t) - f_j^{\mathrm{eq}}(\vec{x},t)], \tag{11}$$

where $\mathbf{M}$ is a transformation matrix [69] and $\mathbf{S}$ is the diagonal matrix containing the relaxation rates for the D3Q19 lattice model. The MRT collision operator transforms the populations to moment space via a transformation matrix $\mathbf{M}$, where the hydrodynamic moments are relaxed individually using a relaxation matrix $\mathbf{S}$. The relaxed moments are then transformed back to population space using $\mathbf{M}^{-1}$ matrix. The relaxation matrix $\mathbf{S}$ and relaxation rates s_i used in the present study are given by [70]

$$S = \mathrm{diag}[0, s_1, s_2, 0, s_4, 0, s_4, 0, s_4, s_9, s_{10}, s_9, s_{10}, s_{13}, s_{13}, s_{13}, s_{16}, s_{16}, s_{16}], \tag{12}$$

$$s_1 = s_2 = s_9 = s_{10} = s_{13} = \frac{1}{\tau}, \quad s_4 = s_{16} = \frac{8(2-s_1)}{8-s_1}. \tag{13}$$

The relaxation time τ is computed locally at every time step using the local viscosity of the fluid mixture, which is obtained by taking a weighted harmonic mean of the viscosities of the two fluids as given by [71]

$$\frac{1}{\mu(\vec{x},t)} = \frac{1+\rho_N(\vec{x},t)}{2\mu_R(\vec{x},t)} + \frac{1-\rho_N(\vec{x},t)}{2\mu_B}. \tag{14}$$

Here μ_R and μ_B are the viscosities of the individual fluids (red and blue) and $\rho_N(\vec{x},t)$ is the local phase field as defined later in Eq. (19). The shear-dependent viscosity of the continuous phase $[\mu_R(\vec{x},t)]$ is computed using the CY model given in Eq. (2). The second invariant of the strain rate tensor $|\dot{\gamma}|$ (to be used in the CY model) is computed at every lattice site using [72,73]

$$\dot{\gamma}_{\alpha\beta}(\vec{x},t) = -\frac{1}{2\rho c_s^2}\sum_i e_{i\alpha}e_{i\beta}\sum_j(\mathbf{M}^{-1}\mathbf{S}\mathbf{M})_{ij}\left[f_j(\vec{x},t) - f_j^{\mathrm{eq}}(\vec{x},t) + \frac{F_j\Delta t}{2}\right], \tag{15}$$

$$|\dot{\gamma}| = \sqrt{2\dot{\gamma}_{\alpha\beta}\dot{\gamma}_{\alpha\beta}}. \tag{16}$$

C. Color-gradient multiphase model

Several multiphase and multicomponent models have been developed within the LBM, of which the most widely used include color-gradient [74], interparticle potential [75], and free-energy [76] models. In the present study, the color-gradient method has been used as it offers advantages such as low spurious velocities at the interface, a tunable interfacial tension, and a noniterative calculation process. The two-phase color-gradient multicomponent model begins by assigning a separate color (red or blue) for each of the two fluids, which are then represented by their own distribution functions ($f_{i,R}$ and $f_{i,B}$, respectively). Thereafter, the distribution function f_i for the "color-blind" fluid is defined as a sum of the two distributions as

$$f_i = f_{i,B} + f_{i,R}. \tag{17}$$

The interfacial tension force $\vec{F}^{\mathrm{ext}}$, modeled using the concept of continuum surface force [77], is given by

$$\vec{F}^{\mathrm{ext}}(\vec{x},t) = -\tfrac{1}{2}\kappa\sigma\vec{\nabla}\rho_N(\vec{x},t), \tag{18}$$

where $\rho_N(\vec{x}, t)$ is the local phase field, κ is the local curvature of the interface, and σ is the interfacial tension coefficient. The local phase field $\rho_N(\vec{x}, t)$ is defined as

$$\rho_N(\vec{x}, t) = \frac{\rho_R - \rho_B}{\rho_R + \rho_B}, \tag{19}$$

where $-1 \leqslant \rho_N \leqslant 1$. The local curvature of the interface $\kappa(\vec{x}, t)$ is computed using

$$\kappa(\vec{x}, t) = \frac{1}{R} = -\vec{\nabla}_s \cdot \vec{n}, \tag{20}$$

$$\vec{n}(\vec{x}, t) = -\frac{\vec{\nabla}\rho_N}{|\vec{\nabla}\rho_N|}, \tag{21}$$

$$\vec{\nabla}_s = (\mathbf{I} - \vec{n}\vec{n}) \cdot \vec{\nabla}, \tag{22}$$

where R is the radius of curvature of the local interface, $\vec{n}$ is the local unit normal vector to the interface, $\mathbf{I}$ is the identity matrix, and $\vec{\nabla}_s$ is the surface gradient operator. The partial derivatives involved in the computation of the normal vector and local curvature are computed based on the discretization formulation given by

$$\frac{\partial \phi}{\partial x_\alpha} = \frac{1}{c_s^2} \sum_i \phi(\vec{x} + \vec{e}_i) e_{i\alpha} w_i, \tag{23}$$

where ϕ is any spatially varying function. Using the forcing scheme [65] within the framework of the MRT formulation, $\vec{F}^{\text{ext}}$ given by Eq. (18) is incorporated in the LBE using [78]

$$\bar{F}_i = w_i \left[\frac{\vec{e}_i - \vec{u}}{c_s^2} + \left(\frac{\vec{e}_i \cdot \vec{u}}{c_s^4} \right) \vec{e}_i \right] \cdot \vec{F}^{\text{ext}}, \tag{24}$$

$$F_i = \left[\mathbf{M}^{-1} \left(\mathbf{I} - \frac{\mathbf{S}}{2} \right) \mathbf{M} \right]_{ij} \bar{F}_j, \tag{25}$$

where F_i is the source term in the LBE (4).

D. Implementation

In the case of a color-gradient multiphase model, the LBE (4) is solved by decomposing it into three distinct steps, collision, recoloring, and streaming, which are performed in succession. The collision (or relaxation) operation is performed using

$$f_i^*(\vec{x}, t) = f_i(\vec{x}, t) + \Omega_i(\vec{x}, t) + F_i(\vec{x}, t), \tag{26}$$

where f_i^* is the postcollision total distribution function. The collision operator and the source term, as described above, are computed at every time instant and lattice site using Eqs. (12)–(16) and Eqs. (17)–(25), respectively. Following the collision step, the recoloring step is performed in which the postcollision distribution functions for the individual fluids are obtained from the total distribution function using [79]

$$f_{i,R}^*(\vec{x}, t) = \frac{\rho_R}{\rho_R + \rho_B} f_i^*(\vec{x}, t) + \beta w_i \frac{\rho_R \rho_B}{\rho_R + \rho_B} \frac{\vec{e}_i \cdot \vec{\nabla}\rho_N}{|\vec{\nabla}\rho_N|}, \tag{27}$$

$$f_{i,B}^*(\vec{x}, t) = \frac{\rho_B}{\rho_R + \rho_B} f_i^*(\vec{x}, t) - \beta w_i \frac{\rho_R \rho_B}{\rho_R + \rho_B} \frac{\vec{e}_i \cdot \vec{\nabla}\rho_N}{|\vec{\nabla}\rho_N|}. \tag{28}$$

Finally, in the streaming (or propagation) step the postcollision distribution function of both the fluids is propagated to the neighboring site as given by

$$f_{i,k}(\vec{x} + \vec{e}_i \Delta t, t + \Delta t) = f_{i,k}^*(\vec{x}, t). \tag{29}$$

TABLE I. Physical properties and flow rates of the fluids used in the two experiments. The viscosity of the xanthan solution mentioned in the table represents its zero-shear viscosity. All the properties are measured at 25 °C.

Experiment	Fluid: Continuous phase	Fluid: Dispersed phase	Viscosity (mPa s) μ_c	Viscosity (mPa s) μ_d	Density (kg m^{-3}) ρ_c	Density (kg m^{-3}) ρ_d	Interfacial tension (mN m^{-1}) σ	Flow rate (μl min^{-1}) Q_c	Flow rate (μl min^{-1}) Q_d
I	85% glycerol-water solution + 0.1% Triton X-100	silicone oil	90	25	1218	950	6.25 ± 0.2	85	8.5
II	800-ppm xanthan solution + 0.1% Triton X-100	silicone oil	87	25	1000	950	6.25 ± 0.2	85	8.5

IV. EXPERIMENTAL SETUP AND MATERIALS

The numerical investigation is complemented by an experimental study to validate the simulation results. Droplets are produced inside a T-junction microchannel fabricated by micromilling on a poly(methyl methacrylate) (PMMA) substrate of 2 mm thickness. The fabricated microchannels (both main and side channels) have a square cross section with each side measuring 500 μm. The milled PMMA chip with the microchannels is sealed with another flat PMMA sheet of 2 mm thickness by clamping and heating them together in a vacuum oven at 155 °C for 45 min. The experiments are performed with silicone oil as the dispersed phase fluid (Newtonian), while two different fluids are used as continuous phases. An 85% aqueous solution of glycerol is used as a Newtonian continuous phase, while an 800-ppm aqueous xanthan solution (molecular weight 2.7×10^6 g mol^{-1}, Sigma Aldrich G1253) serves as the shear-thinning continuous phase. The 800-ppm xanthan solution is specifically chosen because at low concentrations it predominantly exhibits shear-thinning behavior with negligible elasticity [80]. This is because, at concentrations below 1000 ppm, the first normal stress difference is almost absent in xanthan solutions [81].

The physical properties of the continuous and the dispersed phase fluids are measured at 25 °C and are given in Table I. The rheology of the two continuous phase fluids is characterized using a cone and plate rheometer (AntonPaar MCR 302) and the measured rheological data are shown in Fig. 3. As expected, the glycerol solution shows a shear-rate-independent viscosity, while the viscosity of the xanthan solution decreases with an increase in the shear rate. The shear-thinning viscosity of the xanthan solution is quantified by fitting the rheological data with Eq. (2). The obtained fitting parameters listed in Table II are in good agreement with those reported in the literature [81,82]. A surfactant (Triton X-100) is added to both the glycerol and the xanthan solutions to improve their wetting with the channel walls. The interfacial tension between the silicon oil and the two continuous phase fluids is measured using a pendant drop technique [83]. The pendant droplets of the two aqueous solutions are made inside an oil-filled cuvette and their images are acquired using a goniometer (Dataphysics OCA 15EC) and are then imported to an open-source

TABLE II. The CY model fitting parameters for the two continuous phase fluids used in the experiments.

Fluid	n	λ
85% glycerol–water solution	1	0
800-ppm xanthan solution	0.53	5.5

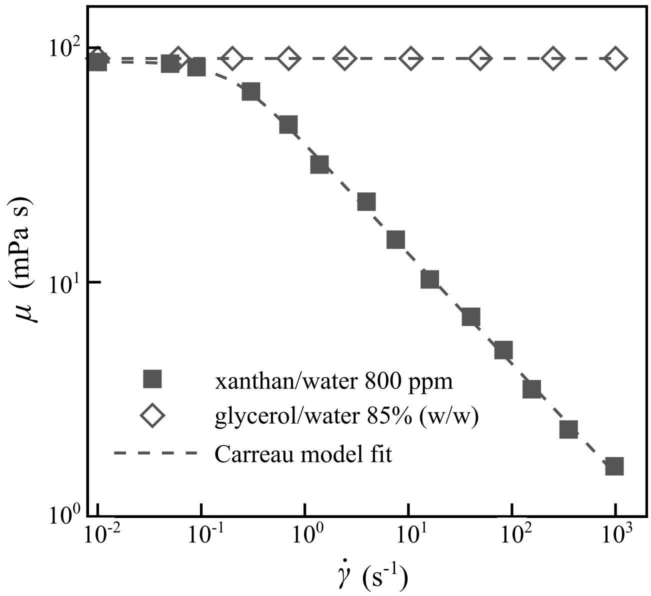

FIG. 3. Variation of viscosity with the shear rate for the two fluids used as continuous phases in the experiments. The symbols represent the experimentally measured values, while the dashed line depicts the CY model fit. The measured values are at 25 °C.

software Opendrop [84]. The software fits the droplet profiles with the axisymmetric solutions of the Young-Laplace equation to measure the interfacial tension between the liquid-liquid interface.

The droplet formation experiments are conducted by injecting the dispersed and the continuous phases through the side and the main channel, respectively. The flow rates are controlled by using two independent syringe pumps (KD Scientific Legato 110 series), which are connected with the microchannels using pressure monitoring tubing. Before injecting the dispersed phase, the microchannel walls are primed with the continuous phase. The droplet formation is observed using an inverted microscope (Nikon Eclipse Ti-U, Japan) with a 4× objective lens and the data are recorded using a CCD camera (PCO pixelfly) mounted on the inverted microscope.

V. RESULTS AND DISCUSSION

In this section the simulation and experimental results of the droplet formation phenomenon in a shear-thinning continuous phase are presented. First, the grid independence test and the validation of the numerical results for the current problem are presented in Sec. V A. Next, simulation results showing the role of the shear-thinning continuous phase on the droplet size are presented and discussed in Sec. V B. Thereafter, the dynamics of the droplet formation is analyzed and explained in Sec. V C. Finally, a brief study of transitions between different droplet flow regimes in a shear-thinning continuous phase is described in Sec. V D.

A. Grid independence test and validation of numerical results

A grid independence test is performed to determine the optimum grid size for the computational domain. Three different Cartesian grids with a discretization of $N_x \times N_y \times N_z$, i.e., $121\Delta x \times 21\Delta y \times 11\Delta z$, $242\Delta x \times 42\Delta y \times 22\Delta z$, and $484\Delta x \times 84\Delta y \times 44\Delta z$, are considered. The grids are numbered in increasing order of resolution: coarse, medium, and fine grids labeled as grids I, II, and III, respectively. A Newtonian system of fluids with viscosity and flow rate ratios each equal to $1/8$ is considered and the normalized droplet volume is determined for five evenly spaced capillary

TABLE III. Results of the grid independence test performed on three grids (grids I–III), with increasing spatial resolution.

Ca	Normalized droplet volume $\bar{V}$			Change in $\bar{V}$ for grid I with respect to grid III (%)	Change in $\bar{V}$ for grid II with respect to grid III (%)
	Grid I	Grid II	Grid III		
0.01	1.132	1.034	1.017	11.3	1.7
0.02	0.805	0.705	0.691	16.5	2.0
0.03	0.555	0.514	0.503	10.3	2.2
0.04	0.515	0.454	0.441	16.7	2.9
0.05	0.413	0.382	0.371	11.3	2.9

numbers between 0.01 and 0.05. These five simulations have been performed for each of the three grids and the results are tabulated in Table III.

As is evident from Table III, the relative percentage change in the droplet volume is less than 3% on increasing the grid resolution from medium to fine for all the cases considered. Consequently, in order to strike a balance between computational load and accuracy, grid II of medium resolution ($242 \times 42 \times 22$) is employed to obtain the simulation results presented henceforth. The simulations performed for conducting the grid independence test have been further used to verify the numerical methodology for a Newtonian system of fluids. Figure 4 shows a comparison between the simulation results obtained using the present LBM and those obtained using the phase-field method used by de Menech *et al.* [29]. It can be observed that the normalized droplet volumes computed from both methods are in good agreement with each other, with a maximum error of 5% for Ca = 0.01.

Having benchmarked the present numerical method for Newtonian fluids, the experimental results obtained in the present study are used to test the capability of the numerical model in simulating the formation of a Newtonian droplet in a non-Newtonian continuous phase exhibiting a purely viscous shear-thinning behavior. Two separate experiments are performed following the methodology detailed in Sec. IV. The details of the two experimental cases are given in Table I.

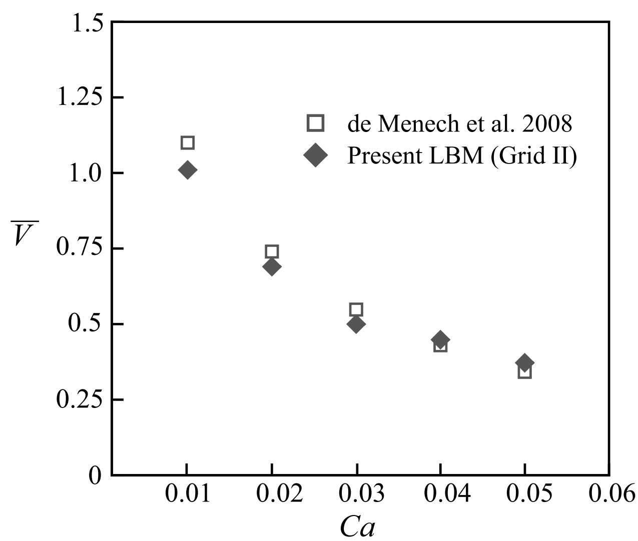

FIG. 4. Comparison of the normalized droplet volume from the present LBM simulations with those obtained from the phase-field simulations of de Menech *et al.* [29]. The fluids used in the simulations are Newtonian with a viscosity and flow rate ratio of 1/8.

TABLE IV. Dimensionless parameters for the two experimental cases.

Experiment	Capillary number Ca	Flow rate ratio Q	Viscosity ratio ϕ	Carreau number Cr	Power-law index n
I	0.0816	0.1	0.277	0	1
II	0.0788	0.1	0.287	62.33	0.53

In the first experiment, a Newtonian continuous phase comprising a 85% glycerol–water solution is used, while a shear-thinning continuous phase made up of an 800-ppm xanthan solution is employed in the second. The choice of the two continuous phases has been made such that the zero-shear viscosity of the shear-thinning fluid is nearly equal to the constant viscosity of the Newtonian fluid. This results in similar capillary numbers for the two experiments when operated at the same values of inlet flow rates. The values of the dimensionless parameters computed from the flow rates and physical properties of the two fluids are given in Table IV. It is evident that, besides the shear-thinning parameters (n and Cr), all other dimensionless parameters are the same for the two experimental cases. Therefore, any difference in the droplet formation process between the two experimental cases can be expected to be dictated by the shear-thinning property of the continuous phase. It should be noted that the effect of gravity can be ignored for the present droplet formation experiments as gravity acts in a direction orthogonal to the plane in which droplet flow process occurs. Moreover, the Bond number Bo, which measures the importance of gravitational force compared to capillary force, is much less than unity for the experiments shown in this work (Bo $= 0.1$ and 0.02 for experiments I and II, respectively).

Qualitative comparisons of the outcomes obtained from the simulations and the experiments for the Newtonian and the shear-thinning continuous phase are shown in Figs. 5(a) and 5(b), respectively. The experimental observations show an increase in the droplet size along with a change in the droplet shape from spherical to that resembling a plug on changing the nature of the continuous phase from Newtonian [Fig. 5(a i)] to shear thinning [Fig. 5(b i)] (keeping all other dimensionless parameters unchanged). Simulations corresponding to the two cases of experimental conditions are performed and the outcomes obtained for the Newtonian and the shear-thinning continuous phase are shown in Figs. 5(a ii) and 5(b ii), respectively. It can be noticed that the numerical solutions show a very similar droplet formation process and the resultant droplet size compared to the experimental observations for both types of continuous phase fluids. It is therefore concluded that the shear-thinning property associated with the continuous phase has a significant influence on the droplet formation process and the resultant droplet size, an effect very well captured by the present numerical model.

B. Effect of shear-thinning parameters n and Cr

Having benchmarked the numerical model with previous numerical studies and validated with experimental data, a systematic investigation of the effect of shear-thinning parameters of the continuous phase on the process of droplet formation is carried out. To this end, the shear-thinning parameters, namely, the power-law index n and the Carreau number Cr, are varied in the range $0.3 \leqslant n \leqslant 1$ and $0.01 \leqslant \mathrm{Cr} \leqslant 100$, for two different values of the capillary number Ca $= 0.05$ and 0.1. Apart from Ca, Cr, and n, the values of all other dimensionless parameters in Eq. (29) are kept constant throughout the parametric study. The aspect ratio and the width ratio are taken as $\Gamma = 1$ and $\Lambda = 1$, respectively, while the viscosity ratio, flow rate ratio, and Reynolds number are set as $\phi = 0.1$, $Q = 0.1$, and Re $= 0.1$, respectively, for all the numerical results presented henceforth.

A sequence of images illustrating the droplet formation process for three different values of n are shown in Figs. 6(a)–6(c) and the normalized droplet volume is plotted as a function of n for Ca $= 0.05$ and 0.1 in Fig. 6(d). It is observed that the droplet volume increases for fluids having lower values of n for both values of Ca. The droplet formation process shown in Figs. 6(a)–6(c)

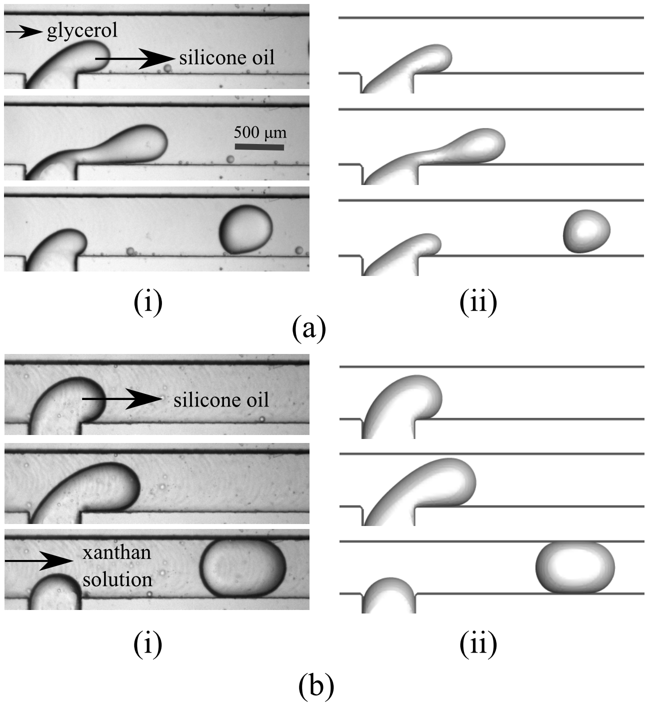

FIG. 5. Comparison of the visualization of the droplet formation process between (i) the experimental observations and (ii) the simulation results. (a) Comparison corresponding to case I, involving Newtonian fluid as the continuous phase. (b) Comparison corresponding to case II, involving shear-thinning fluid as the continuous phase. The dimensionless parameters corresponding to cases I and II are tabulated in Table IV.

indicates that the higher the shear-thinning degree of the continuous phase (or lower the value of n), the greater the volume that the incoming dispersed phase thread occupies in the main channel before pinching off from the T junction. Additionally, the shape of the droplet changes from spherical to plug shaped, indicating a shift in the droplet formation regime from dripping to squeezing for lower values of n.

The effect of Cr on the process of droplet formation is shown in Fig. 7. Similar to the analysis for n, a series of snapshots describing the formation of droplets for different values of Cr is shown, and the normalized droplet volume as a function of Cr is plotted for $\mathrm{Ca} = 0.05$ and 0.1. The droplet volume is observed to increase with Cr in a manner which is similar for both values of Ca, which suggests that the effect of Cr on the droplet volume may be independent of the capillary number in the range $0.05 \leqslant \mathrm{Ca} \leqslant 0.1$. The droplet size increases only marginally for $\mathrm{Cr} \leqslant 0.1$, beyond which the increase is appreciable. This can be attributed to the fact that the continuous phase behaves almost like a Newtonian fluid for lower values of Cr. However, for $\mathrm{Cr} \geqslant 0.1$ the transition from Newtonian to shear-thinning behavior begins at progressively lower values of shear rates which are experienced in a microchannel. Consequently, the shear thinning experienced by the continuous phase extends over a wider range of shear rates, leading to the formation of larger droplets.

Along with the increase in the droplet size, a gradual change in the shape of the droplet is also observed for fluids having higher values of Cr. It can be seen by comparing Figs. 7(a) and 7(c) that the shape of the droplet changes from spherical to that resembling a plug confined by the walls of the main channel as the value of Cr increases from 1 to 100. Such an effect, which was also observed for lower values of n, further suggests that the dynamics of droplet formation shifts from a shear-dominated dripping regime to a pressure-dominated squeezing regime for continuous

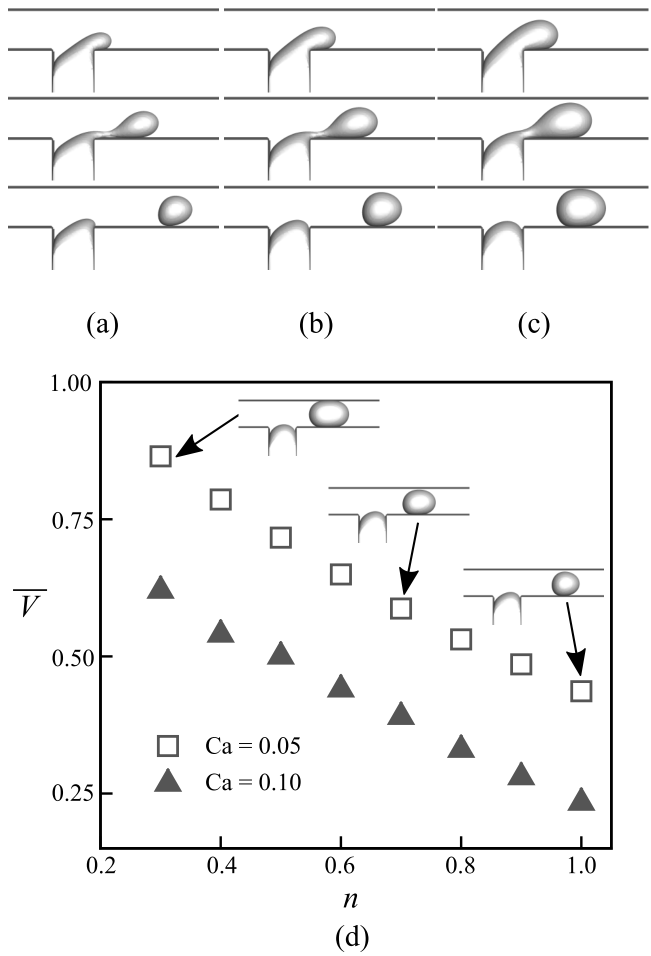

FIG. 6. Simulation results illustrating the effect of power-law index n of the continuous phase on the process of droplet formation at a T junction. A two-dimensional visualization of the process of droplet formation is shown on the x-y plane for $\mathrm{Cr} = 1$, $\mathrm{Ca} = 0.1$, and (a) $n = 1.0$, (b) $n = 0.7$, and (c) $n = 0.3$. (d) Variation of normalized droplet volume with n for $\mathrm{Cr} = 1$, with the insets showing the visuals of the droplet produced.

phase fluids having a higher shear-thinning property (lower n and higher Cr). Intuitively, such a shift in the dynamics of droplet formation could be caused due to the reduction in the viscous resistance offered by the continuous phase on the dispersed phase as the shear-thinning tendency of the continuous phase becomes greater. As a result, the interfacial forces resisting the deformation of the interface become more dominant than the shear stresses, and the droplet breakup is achieved due to the buildup of upstream pressure rather than the competition between the shear stress and the interfacial tension. The results presented in the subsequent section will further corroborate this hypothesis about the mechanism of droplet formation in a shear-thinning continuous phase.

The increase in the normalized droplet volume for a shear-thinning continuous phase with respect to a Newtonian continuous phase $\bar{V} - \bar{V}_{n=1}$ is normalized with $1 - n$ and is given by the function $\psi = (\bar{V} - \bar{V}_{n=1})/(1 - n)$. Figure 8 shows the variation of ψ with Cr for $n = 0.3$, 0.5, and 0.7 and at $\mathrm{Ca} = 0.05$ and 0.1. It can be observed that all the numerical data for different values of n and Ca collapse on a single curve ($\psi = 0.22 \ln \mathrm{Cr} + 0.52$) for over three orders of magnitude of Cr

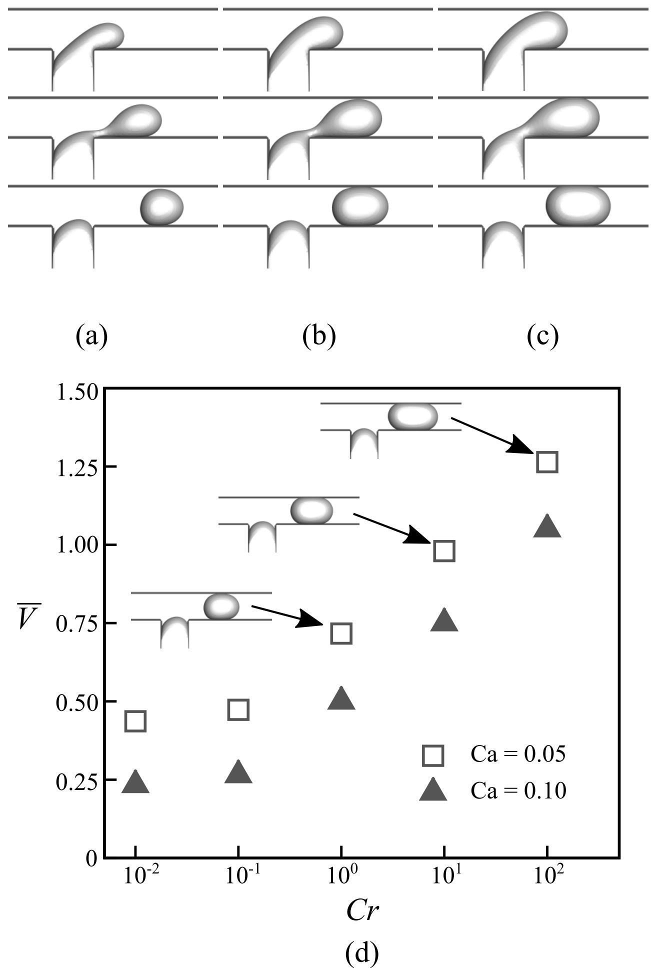

FIG. 7. Simulation results illustrating the effect of Carreau number Cr on the process of droplet formation at a T junction. The two-dimensional visualization of the process of droplet formation is shown on the x-y plane for $n = 0.5$, Ca $= 0.1$, and (a) Cr $= 1$, (b) Cr $= 10$, and (c) Cr $= 100$. (d) Variation of normalized droplet volume with Cr for $n = 0.5$, with the insets showing the visuals of the droplet produced.

($0.1 \leqslant$ Cr $\leqslant 100$). It can also be noticed that for a particular Cr, ψ remains nearly independent of n and Ca. This suggests that the increase in the normalized droplet volume for shear-thinning fluids ($\bar{V} - \bar{V}_{n=1}$) is linearly proportional to $1 - n$ and is independent of Ca for the range of n and Cr considered.

C. Droplet formation dynamics

In this section, a deeper mechanistic analysis of the dynamics of droplet formation in a shear-thinning continuous phase is reported to get a better understanding of the non-Newtonian effects on the droplet shape and size. The pressure, interfacial force, and shear force are the three main forces which act on the dispersed phase as it emerges into the main channel [29]. The pressure and the shear stress act to squeeze and stretch the emerging dispersed phase thread, respectively, while the interfacial tension tends to resist this deformation. The dynamics of droplet formation is therefore governed by the force which overcomes the resistive interfacial tension and causes the interface to

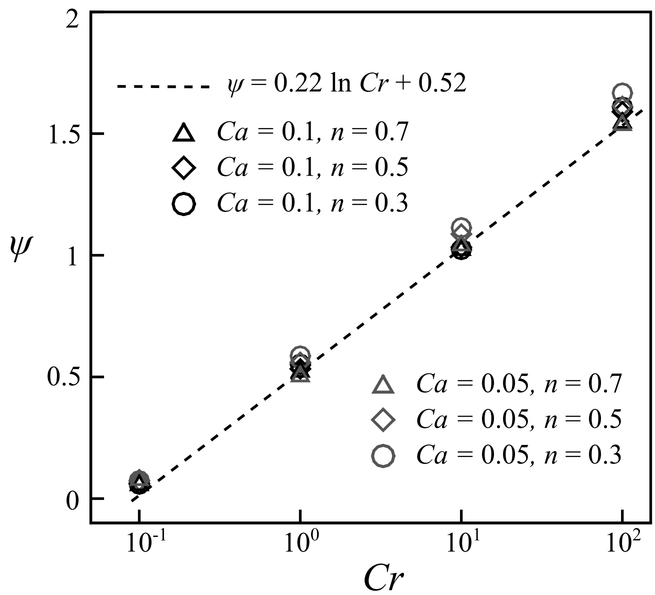

FIG. 8. Variation of $\psi = (\bar{V} - \bar{V}_{n=1})/(1 - n)$ with the Carreau number Cr for three different values of power-law index $n = 0.3$, 0.5, and 0.7 and at two different values of capillary number Ca = 0.05 and 0.1. Symbols represent the simulation results, while the dashed line corresponds to a logarithmic correlation that fits the numerical data.

break. The buildup of the pressure force upstream of the T junction and the shear stress exerted by the continuous phase on the emerging droplet are investigated for different cases of shear-thinning parameters and the corresponding numerical results are presented.

The immediate effect of using a shear-thinning fluid as the continuous phase is the attenuation of the local viscosity of the continuous phase as it flows through the microchannel. The distribution of normalized local viscosity is plotted on the x-y midplane for three representative cases of n and Cr, as shown in Figs. 9(a) and 9(b), respectively. The droplets are shown at the correspondingly same states of their formation cycle, i.e., when the dispersed phase has protruded out to a maximum size into the main channel and its neck has just started to be squeezed. The local viscosities are normalized with the zero-shear viscosity. As expected, for a Newtonian continuous phase ($n = 1$) the normalized viscosity throughout the channel remains constant (except near the interface, which is due to the diffused nature of the numerical method). However, for a shear-thinning continuous phase the normalized viscosity varies across the channel. Furthermore, the attenuation in the local viscosity across the channel is enhanced for continuous phase fluids having lower n or higher Cr.

Figures 9(c) and 9(d) show the variation of the normalized local viscosity along the cross section of the main channel for different values of n and Cr, respectively. The viscosity variation is plotted at a location upstream of the junction as shown by the dotted line AA' in the inset image of Fig. 9(c). For all the cases involving a shear-thinning continuous phase, the viscosity is reduced symmetrically on moving away from the center of the channel. The reduction in viscosity when n from 0.7 to 0.3 is observed to be higher near the walls as compared to the center. This is attributed to the fact that the fluid experiences shear thinning only at a certain distance away from the center of the channel where the shear rate is sufficiently high, for the Cr considered. Hence the central region (having lower shear rates) remains unaffected, while the region near the channel walls (where the shear rates are higher) experiences a significant reduction in viscosity for fluids having lower values of n. On the other hand, as Cr goes from 1 to 10, the decrease in the viscosity is appreciable near the center also due to the onset of shear thinning at relatively lower shear rates.

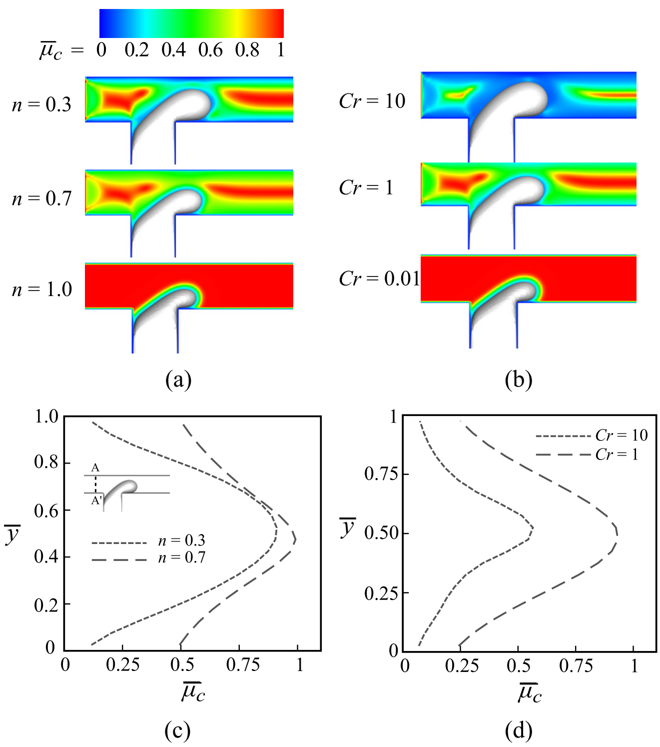

FIG. 9. Contours of normalized dynamic viscosity of the continuous phase $\bar{\mu}_c$ for (a) $n = 0.3$, 0.7, and 1.0 at $\mathrm{Cr} = 1$ and $\mathrm{Ca} = 0.1$ and (b) $\mathrm{Cr} = 0.01$, 1, and 10 at $n = 0.5$ and $\mathrm{Ca} = 0.1$. The contours are shown on the x-y plane, which is midway between the top and bottom walls. (c) and (d) Variation of $\bar{\mu}_c$ along the cross section of the main channel at a location marked by the dotted line in the inset image of (c), corresponding to the cases considered in (a) and (b), respectively. The dynamic viscosity of the continuous phase is normalized by its zero-shear viscosity $\mu_{c,0}$ and the distance along the cross section of the main channel y is scaled with the width of the main channel W_c.

The observed change in the local viscosity of the continuous phase has a subsequent influence on the shear-stress distribution. Contours of normalized shear stress ($\bar{\tau}_{xy}$) are shown in Figs. 10(a) and 10(b) for three representative cases of n and Cr. For all the cases considered, the droplets are visualized at the same stage of their formation process as was described earlier. A substantial decrease in the magnitude of shear stress can be noticed throughout the channel as n decreases from 1.0 to 0.3 or when Cr increases from 0.01 to 100. To specifically ascertain the shear-thinning effect on the shear stress experienced by the emerging droplet, the normalized shear stress is also plotted along the interface of the dispersed phase ($\bar{\tau}_s$) as shown in Figs. 10(c) and 10(d) for different values of n and Cr, respectively. The area under the shear-stress profile along the interface can be considered as the measure of the total shear force experienced by the emerging droplet, which as observed from Figs. 10(c) and 10(d) is least for the most shear-thinning continuous phase ($\mathrm{Cr} = 100$ and $n = 0.3$). It can therefore be concluded that the contribution of the shear forces to the droplet breakup process becomes progressively less significant as the shear-thinning tendency of the continuous phase is enhanced.

After having investigated the role of shear stress, the upstream pressure force is analyzed for its significance in controlling the dynamics of droplet formation in a shear-thinning continuous phase. Figure 11 shows the temporal evolution of pressure in the continuous phase as the droplet goes through various stages of its formation in a shear-thinning fluid. The buildup of pressure is computed

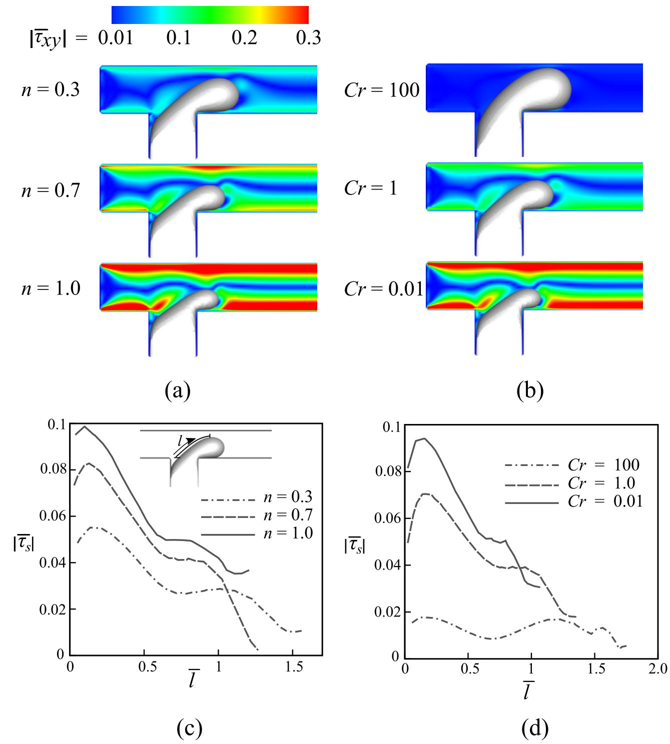

FIG. 10. Contours of normalized shear stress $\bar{\tau}_{xy}$ for (a) $n = 0.3$, 0.7, and 1.0 at $\mathrm{Cr} = 1$ and $\mathrm{Ca} = 0.1$ and (b) $\mathrm{Cr} = 0.01$, 1, and 100 at $n = 0.5$ and $\mathrm{Ca} = 0.1$. The contours are shown on the x-y plane, which is midway between the top and bottom walls. (c) and (d) Variation of the normalized shear stress along the length of the droplet interface $\bar{\tau}_s$ [as represented in the inset image of (c)], corresponding to the cases considered in (a) and (b), respectively. The shear stress is normalized by σ/W_c, while the length along the interface is scaled with the width of the main channel W_c.

at a point upstream of the T junction with respect to a reference pressure (the outlet pressure) as shown in the inset of Fig. 11(a). It should be noted that the outlet pressure remains fixed in all the simulations reported here. The pressure has been normalized with the minimum pressure difference as observed during several cycles of droplet formation. Temporal pressure profiles obtained for different values of n and Cr are shown in Figs. 11(a) and 11(b), respectively. It is observed that the pressure fluctuates in a periodic manner, the amplitude of which increases with an increase in the value of Cr and a decrease in the value of n. Additionally, the period of pressure fluctuations decreases with an increase in the shear-thinning tendency of the continuous phase. Since the period of a pressure fluctuation wave represents the droplet formation time, an increase in its value is indicative of an increase in the droplet size and a decrease in the formation frequency.

The change in the amplitude of the pressure fluctuation wave with the shear-thinning parameters of the continuous phase can be better understood by examining the process of droplet formation. As shown in Figs. 11(c) and 11(d), the droplet shapes for different values of n and Cr are compared with each other at five different time instances shown on their pressure profile. These points are chosen such that they cover one cycle of the pressure fluctuation wave. In general, the droplet formation cycle can be divided into filling stages (state 1 to state 3) and breaking stages (state 3 to state 5). The filling and breaking times correspond to the time durations of the two stages of droplet formation as shown in Fig. 11(b). During the filling stage, the upstream pressure rises gradually as the dispersed phase fills the cross section of the main channel obstructing the flow of the continuous phase, while

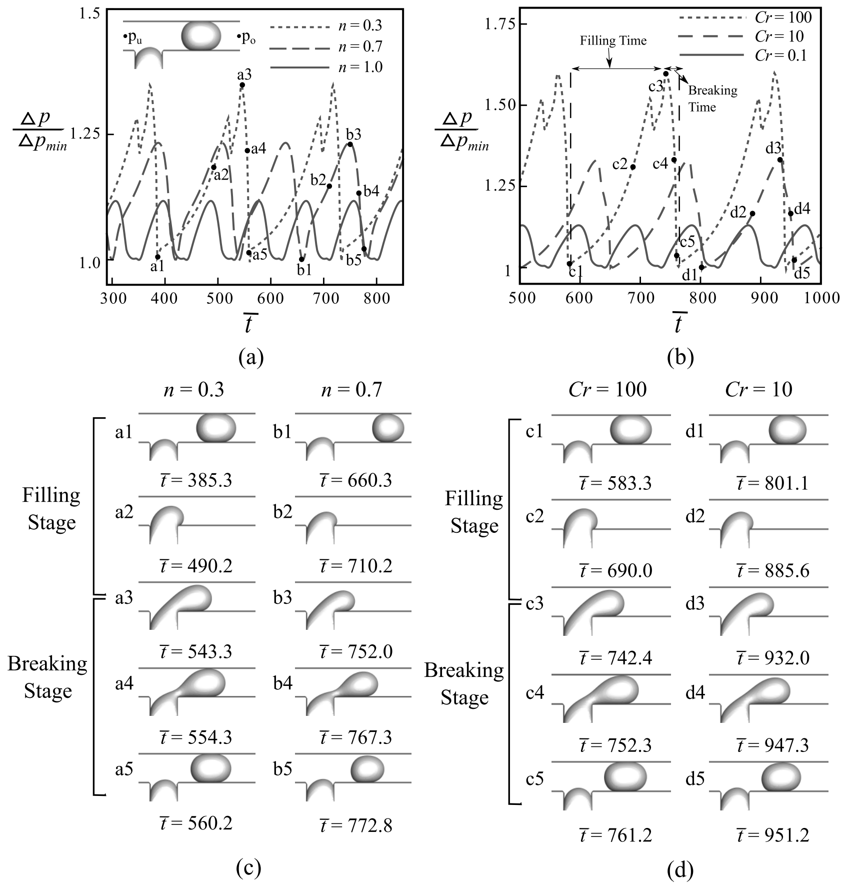

FIG. 11. Time evolution of pressure buildup for the process of droplet formation in a shear-thinning continuous phase. Pressure profiles are shown for (a) different values of n, Cr $= 1$, and Ca $= 0.05$ and (b) different values of Cr, $n = 0.7$, and Ca $= 0.05$. The pressure buildup $\Delta p = p_u - p_o$ is computed by subtracting the constant outlet pressure p_o from the upstream pressure p_u, as marked in the inset of (a). The pressure buildup is normalized by its minimum value Δp_{min} observed during several cycles of droplet formation and the time is scaled using $t_0 = \mu_{c,0} W_c/\sigma$ such that $\bar{t} = t/t_0$. Different stages of the droplet formation process are visualized in (c) and (d), which correspond to the instances marked on the pressure profiles in (a) and (b), respectively.

during the breaking stage there is an abrupt decrease in the upstream pressure as the continuous phase squeezes the neck of the dispersed phase. Once the interface is broken and the breaking stage is over, the pressure begins to rise again as the dispersed phase starts to penetrate the main channel and the cycle repeats. The amplitude of pressure fluctuation can therefore be considered as a measure of blockage of the main channel caused by the dispersed phase. It should be noted that the minor peak in the pressure buildup curve seen during the filling time of the droplet for $n = 0.3$ and Cr $= 100$ in Figs. 11(a) and 11(b), respectively, arises when a previously formed droplet begins to exit the channel [37]. Since the pressure drop across the channel is dependent on the number of droplets in the channel, a pressure drop is observed when a droplet exits the main channel [85]. The comparison of droplet shapes [for $n = 0.3$ and 0.7 in Fig. 11(c) and Cr $= 10$ and 100 in Fig. 11(d)] shows that the maximum blockage caused by the dispersed phase is greater in a continuous phase with a higher value of Cr or a lower value of n, which results in a larger buildup of the upstream pressure. We conclude that for continuous phases with higher shear-thinning tendency the dynamics

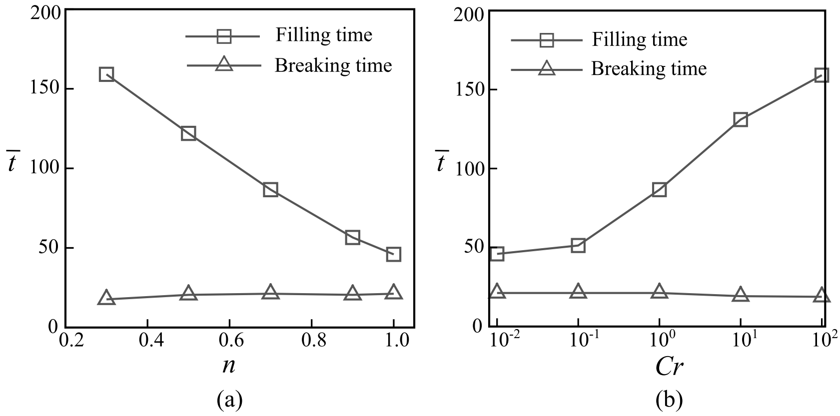

FIG. 12. Plot of the filling and the breaking time in the process of droplet formation as a function of (a) the power-law index n for Cr = 1 and Ca = 0.05 and (b) the Carreau number Cr for $n = 0.7$ and Ca = 0.05.

of droplet formation shifts towards the squeezing regime in which the droplet breakup is governed by the buildup of upstream pressure.

The change in the period of pressure fluctuation cycle observed on varying the shear-thinning parameters is analyzed by quantifying the filling time and the breaking time as a function of n and Cr and is shown in Fig. 12. It is observed that the breaking time remains nearly constant with n and Cr, but the filling time increases for fluids having higher shear-thinning tendency (higher Cr or lower n). This suggests that it is the filling time of the droplet formation process which controls the droplet formation frequency and its size. The breaking time, on the other hand, only depends upon the velocity of the outer fluid [29] and is independent of the nature of the continuous phase.

To get further insight into the dynamics of droplet formation, the time evolution of the upstream pressure buildup and shear-stress distribution is analyzed for cases when similar sized droplets are formed using different shear-thinning continuous phase fluids. Two different cases of the droplet formation process are simulated, designated as cases I and II, with continuous phase fluids having shear-thinning parameters as Cr = 1 and $n = 0.5$ and as Cr = 10 and $n = 0.7$, respectively. The droplets produced in the two cases are of similar sizes with the nondimensional droplet volume computed as 0.72 and 0.74 for cases I and II, respectively. Figures 13(a) and 13(b) show the comparison of the evolution of upstream pressure buildup and shear-stress distribution for the two cases, respectively. The time evolution of the upstream pressure buildup is comparable for the two cases, with the peak pressure being slightly higher in case II due to the marginally larger volume of droplets produced as compared to case I. Furthermore, the shear-stress distribution (shown at the instant of maximum upstream pressure) is also observed to be very similar for the two cases of droplet formation. It can therefore be concluded that for similar-sized droplets produced with different shear-thinning continuous phase fluids, the dynamics of droplet formation remains the same.

D. Transition in droplet flow regimes at high Ca

In this section, simulation results are presented showing the transition between different droplet flow regimes in a shear-thinning continuous phase at high capillary numbers (Ca $\geqslant 0.1$). The flow rate ratio and the viscosity ratio are kept constant as 0.1, while the geometrical parameters such as the aspect ratio and the width ratio are fixed as 1. The range of the capillary numbers considered is $0.1 \leqslant \mathrm{Ca} \leqslant 0.5$, while the power-law index and the Carreau number are varied between $0.3 \leqslant n \leqslant 1.0$ and $0.01 \leqslant \mathrm{Cr} \leqslant 1000$, respectively.

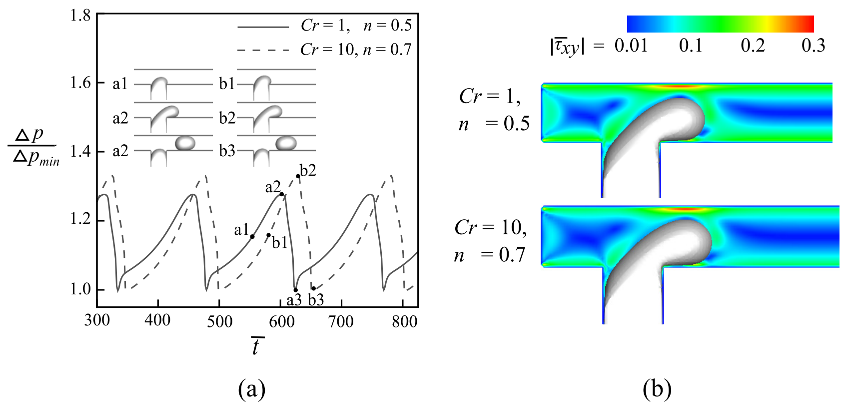

FIG. 13. (a) Time evolution for upstream pressure buildup and (b) normalized shear-stress contours for Cr = 1 and $n = 0.5$ and for Cr = 10 and $n = 0.7$ at Ca = 0.05. The shear-stress contours are shown on the x-y plane, which is midway between the top and bottom walls.

Figure 14 shows the transition in the droplet flow regime from parallel flow to droplet forming at the T junction as the Carreau number of the continuous phase increases. Figures 14(a) and 14(b) show the droplet formation at Ca = 0.2 and 0.5, respectively, for different Cr and $n = 0.5$. For very low values of Cr (Cr = 0.01), a parallel flow is observed for both Ca = 0.2 and 0.5. As the value of Cr increases, the stable jet breaks into droplets at some distance downstream of the T junction. Such a flow pattern is commonly referred to as a droplet in channel (DC) region and is due to the capillary instability setting in the channel [25,32]. With a further increase in Cr, the droplet breakup point moves further upstream to form droplets at the T junction (DTJ). It must be noted that although the droplets formed are nearly spherical in shape in the DTJ flow regime observed at Ca = 0.2 and Cr = 5 and at Ca = 0.5 and Cr = 100 [as shown in Figs. 14(a) and 14(b), respectively], the dispersed phase occupies a significant portion of the main channel before breaking into a droplet. This implies that the pressure effects are not negligible and that both shear stress and upstream pressure buildup are responsible for droplet breakup at the T junction at high Cr and high Ca (Ca > 0.1).

The regime maps shown in Fig. 15 show the three droplet formation regimes as a function of Ca and Cr along with the demarcations which separate them. It can be observed that the critical value of Cr at which the transition of the flow regime from parallel flow (PF) to DC and DC to DTJ occurs increases as the value of Ca is increased, for a particular n. The influence of the power-law index

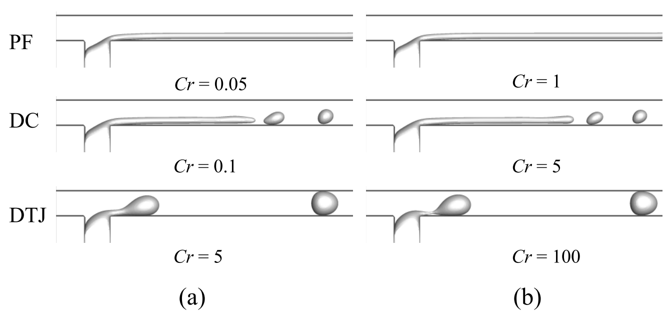

FIG. 14. Visualization of three different regimes of droplet flow observed at different values of Cr and $n = 0.5$ for (a) Ca = 0.2 and (b) Ca = 0.5. Here PF, DC, and DTJ stand for parallel flow, droplet in channel flow, and droplet at the T-junction flow, respectively.

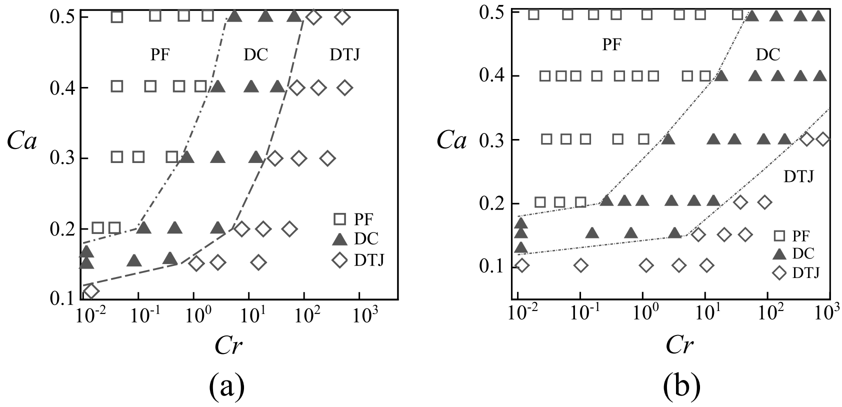

FIG. 15. Regime maps showing the transition between the three droplet flow regimes (i.e., PF, DC, and DTJ) as a function of Ca and Cr for (a) $n = 0.5$ and (b) $n = 0.7$.

on the transition between the three droplet formation regimes is demonstrated by the regime maps for $n = 0.7$ and 0.5, shown in Figs. 15(a) and 15(b), respectively. It can be seen that as the value of n decreases from 0.7 to 0.5, the slope of both PF-DC and DC-DTJ transition lines increases. This indicates that the flow regime transition from parallel to droplet flow occurs at lower values of Cr in the case of a continuous phase with a higher degree of shear thinning (or lower values of n), for a given Ca. In conclusion, for a sufficiently shear-thinning continuous phase, the droplet formation can be facilitated even at high values of Ca, where a parallel flow is observed for a Newtonian continuous phase.

VI. CONCLUSION

In this work, a detailed investigation of the droplet formation phenomenon in a microfluidic T-junction device with a shear-thinning continuous phase has been presented. The droplet formation process was simulated by employing a three-dimensional multicomponent model based on the lattice Boltzmann method. The shear-thinning property of the continuous phase was modeled using a Carreau-Yasuda model. The implemented numerical model was validated with illustrative experimental cases involving both shear-thinning and Newtonian continuous phases. Using the validated numerical model, a parametric study of the effect of rheological parameters (n and Cr) on the droplet size was performed. The ranges of n and Cr considered were $0.3 \leqslant n \leqslant 1$ and $0.01 \leqslant \mathrm{Cr} \leqslant 100$, respectively, for $\mathrm{Ca} = 0.05$ and 0.1. The continuous phase fluids with higher shear-thinning tendency (higher Cr or lower n) produced droplets which were larger in size. Moreover, the increase in the droplet size was accompanied by a consequent change in the droplet shape from spherical to plug shaped. The increase in the normalized droplet volume for a shear-thinning continuous phase (with respect to a Newtonian continuous phase) was shown to be linearly proportional to $1 - n$ and independent of Ca for a particular value of Cr.

To understand the observed variation in the droplet size and shape, the dynamics of droplet formation was analyzed in terms of upstream pressure buildup and the shear stresses acting on the dispersed phase interface. For a continuous phase with a higher shear-thinning tendency, the shear stress acting on the emerging dispersed phase interface was attenuated, along with a simultaneous rise in the amplitude of the pressure fluctuation wave at a location upstream of the T junction. It was therefore concluded that the dynamics of droplet formation progressively shifts towards the pressure-dominated squeezing regime and the shear stress becomes increasingly insignificant for a continuous phase with a higher shear-thinning tendency (or capability). This further explained the observed effect of n and Cr on the droplet size and shape.

The droplet flow regimes at high capillary numbers (Ca $\geqslant 0.1$) with a shear-thinning continuous phase were also studied. The numerical results showed that a transition in the droplet flow regime occurs from parallel flow to droplets forming in the channel to finally droplets being formed at the T junction as the Carreau number of the shear-thinning continuous phase increases. Moreover, this transition occurs at relatively lower values of Cr for fluids having lower values of n.

The results and the analysis presented in this work can significantly aid the understanding of droplet formation and hence assist in the control of the droplet size and frequency in a shear-thinning non-Newtonian continuous phase. A future study investigating the effect of elasticity along with shear thinning is warranted in order to tailor the droplet size and formation regime in continuous phases comprising highly concentrated polymeric solutions which are mainly viscoelastic in nature.

ACKNOWLEDGMENTS

The authors thank the IIT Delhi HPC facility for computational resources.

---

[1] G. F. Christopher and S. L. Anna, Microfluidic methods for generating continuous droplet streams, J. Phys. D **40**, R319 (2007).
[2] S.-Y. Teh, R. Lin, L.-H. Hung, and A. P. Lee, Droplet microfluidics, Lab Chip **8**, 198 (2008).
[3] R. Seemann, M. Brinkmann, T. Pfohl, and S. Herminghaus, Droplet based microfluidics, Rep. Prog. Phys. **75**, 016601 (2011).
[4] P. Zhu and L. Wang, Passive and active droplet generation with microfluidics: A review, Lab Chip **17**, 34 (2017).
[5] Y. Song, J. Hormes, and C. S. S. R. Kumar, Microfluidic synthesis of nanomaterials, Small **4**, 698 (2008).
[6] S. Marre and K. F. Jensen, Synthesis of micro and nanostructures in microfluidic systems, Chem. Soc. Rev. **39**, 1183 (2010).
[7] C.-X. Zhao, Multiphase flow microfluidics for the production of single or multiple emulsions for drug delivery, Adv. Drug Deliver. Rev. **65**, 1420 (2013).
[8] R. Riahi, A. Tamayol, S. A. M. Shaegh, A. M. Ghaemmaghami, M. R. Dokmeci, and A. Khademhosseini, Microfluidics for advanced drug delivery systems, Curr. Opin. Chem. Eng. **7**, 101 (2015).
[9] S. Neethirajan, I. Kobayashi, M. Nakajima, D. Wu, S. Nandagopal, and F. Lin, Microfluidics for food, agriculture and biosystems industries, Lab Chip **11**, 1574 (2011).
[10] V. Blazek and R. A. Caldwell, Comparison of SDS gel capillary electrophoresis with microfluidic lab-on-a-chip technology to quantify relative amounts of 7S and 11S proteins from 20 soybean cultivars, Int. J. Food Sci. Technol. **44**, 2127 (2009).
[11] D.-K. Kang, M. Ali, K. Zhang, S. S. Huang, E. Peterson, M. A. Digman, E. Gratton, and W. Zhao, Rapid detection of single bacteria in unprocessed blood using integrated comprehensive droplet digital detection, Nat. Commun. **5**, 5427 (2014).
[12] D. Pekin, Y. Skhiri, J.-C. Baret, D. Le Corre, L. Mazutis, C. B. Salem, F. Millot, A. El Harrak, J. B. Hutchison, J. W. Larson *et al.*, Quantitative and sensitive detection of rare mutations using droplet-based microfluidics, Lab Chip **11**, 2156 (2011).
[13] D. R. Link, E. Grasland-Mongrain, A. Duri, F. Sarrazin, Z. Cheng, G. Cristobal, M. Marquez, and D. A. Weitz, Electric control of droplets in microfluidic devices, Angew. Chem. Int. Ed. **45**, 2556 (2006).
[14] Z. T. Cygan, J. T. Cabral, K. L. Beers, and E. J. Amis, Microfluidic platform for the generation of organic-phase microreactors, Langmuir **21**, 3629 (2005).
[15] A. B. Theberge, F. Courtois, Y. Schaerli, M. Fischlechner, C. Abell, F. Hollfelder, and W. T. S. Huck, Microdroplets in microfluidics: An evolving platform for discoveries in chemistry and biology, Angew. Chem. Int. Ed. **49**, 5846 (2010).
[16] P. Garstecki, I. Gitlin, W. DiLuzio, G. M. Whitesides, E. Kumacheva, and H. A. Stone, Formation of monodisperse bubbles in a microfluidic flow-focusing device, Appl. Phys. Lett. **85**, 2649 (2004).

[17] P. Garstecki, H. A. Stone, and G. M. Whitesides, Mechanism for Flow-Rate Controlled Breakup in Confined Geometries: A Route to Monodisperse Emulsions, Phys. Rev. Lett. **94**, 164501 (2005).
[18] A. S. Utada, A. Fernandez-Nieves, H. A. Stone, and D. A. Weitz, Dripping to Jetting Transitions in Coflowing Liquid Streams, Phys. Rev. Lett. **99**, 094502 (2007).
[19] C. Cramer, P. Fischer, and E. J. Windhab, Drop formation in a co-flowing ambient fluid, Chem. Eng. Sci. **59**, 3045 (2004).
[20] P. B. Umbanhowar, V. Prasad, and D. A. Weitz, Monodisperse emulsion generation via drop break off in a co-flowing stream, Langmuir **16**, 347 (2000).
[21] S. L. Anna, N. Bontoux, and H. A. Stone, Formation of dispersions using "flow focusing" in microchannels, Appl. Phys. Lett. **82**, 364 (2003).
[22] W. Lee, L. M. Walker, and S. L. Anna, Role of geometry and fluid properties in droplet and thread formation processes in planar flow focusing, Phys. Fluids **21**, 032103 (2009).
[23] A. Gupta, H. S. Matharoo, D. Makkar, and R. Kumar, Droplet formation via squeezing mechanism in a microfluidic flow-focusing device, Comput. Fluids **100**, 218 (2014).
[24] T. Thorsen, R. W. Roberts, F. H. Arnold, and S. R. Quake, Dynamic Pattern Formation in a Vesicle-Generating Microfluidic Device, Phys. Rev. Lett. **86**, 4163 (2001).
[25] P. Guillot and A. Colin, Stability of parallel flows in a microchannel after a T junction, Phys. Rev. E **72**, 066301 (2005).
[26] S. van der Graaf, T. Nisisako, C. G. P. H. Schroën, R. G. M. van der Sman, and R. M. Boom, Lattice Boltzmann simulations of droplet formation in a T-shaped microchannel, Langmuir **22**, 4144 (2006).
[27] P. Garstecki, M. J. Fuerstman, H. A. Stone, and G. M. Whitesides, Formation of droplets and bubbles in a microfluidic T-junction—Scaling and mechanism of break-up, Lab Chip **6**, 437 (2006).
[28] J. H. Xu, S. W. Li, J. Tan, Y. J. Wang, and G. S. Luo, Preparation of highly monodisperse droplet in a T-junction microfluidic device, AIChE J. **52**, 3005 (2006).
[29] M. de Menech, P. Garstecki, F. Jousse, and H. A. Stone, Transition from squeezing to dripping in a microfluidic T-shaped junction, J. Fluid. Mech. **595**, 141 (2008).
[30] G. F. Christopher, N. N. Noharuddin, J. A. Taylor, and S. L. Anna, Experimental observations of the squeezing-to-dripping transition in T-shaped microfluidic junctions, Phys. Rev. E **78**, 036317 (2008).
[31] J. H. Xu, S. W. Li, J. Tan, and G. S. Luo, Correlations of droplet formation in T-junction microfluidic devices: From squeezing to dripping, Microfluid. Nanofluid. **5**, 711 (2008).
[32] A. Gupta, S. M. S. Murshed, and R. Kumar, Droplet formation and stability of flows in a microfluidic T-junction, Appl. Phys. Lett. **94**, 164107 (2009).
[33] V. van Steijn, C. R. Kleijn, and M. T. Kreutzer, Predictive model for the size of bubbles and droplets created in microfluidic T-junctions, Lab Chip **10**, 2513 (2010).
[34] T. Fu, Y. Ma, D. Funfschilling, C. Zhu, and H. Z. Li, Squeezing-to-dripping transition for bubble formation in a microfluidic T-junction, Chem. Eng. Sci. **65**, 3739 (2010).
[35] A. Gupta and R. Kumar, Effect of geometry on droplet formation in the squeezing regime in a microfluidic T-junction, Microfluid. Nanofluid. **8**, 799 (2010).
[36] A. Gupta and R. Kumar, Flow regime transition at high capillary numbers in a microfluidic T-junction: Viscosity contrast and geometry effect, Phys. Fluids **22**, 122001 (2010).
[37] J. Sivasamy, T.-N. Wong, N.-T. Nguyen, and L. T.-H. Kao, An investigation on the mechanism of droplet formation in a microfluidic T-junction, Microfluid. Nanofluid. **11**, 1 (2011).
[38] S. Bashir, J. M. Rees, and W. B. Zimmerman, Simulations of microfluidic droplet formation using the two-phase level set method, Chem. Eng. Sci. **66**, 4733 (2011).
[39] X.-B. Li, F.-C. Li, J.-C. Yang, H. Kinoshita, M. Oishi, and M. Oshima, Study on the mechanism of droplet formation in T-junction microchannel, Chem. Eng. Sci. **69**, 340 (2012).
[40] Y. Yan, D. Guo, and S. Z. Wen, Numerical simulation of junction point pressure during droplet formation in a microfluidic T-junction, Chem. Eng. Sci. **84**, 591 (2012).
[41] S. Bashir, J. M. Rees, and W. B. Zimmerman, Investigation of pressure profile evolution during confined microdroplet formation using a two-phase level set method, Int. J. Multiphas. Flow **60**, 40 (2014).
[42] T. Glawdel, C. Elbuken, and C. L. Ren, Droplet formation in microfluidic T-junction generators operating in the transitional regime. I. Experimental observations, Phys. Rev. E **85**, 016322 (2012).

[43] T. Glawdel, C. Elbuken, and C. L. Ren, Droplet formation in microfluidic T-junction generators operating in the transitional regime. II. Modeling, Phys. Rev. E **85**, 016323 (2012).

[44] P. M. Korczyk, V. van Steijn, S. Blonski, D. Zaremba, D. A. Beattie, and P. Garstecki, Accounting for corner flow unifies the understanding of droplet formation in microfluidic channels, Nat. Commun. **10**, 2528 (2019).

[45] L. Derzsi, M. Kasprzyk, J. P. Plog, and P. Garstecki, Flow focusing with viscoelastic liquids, Phys. Fluids **25**, 092001 (2013).

[46] M. Nooranidoost, D. Izbassarov, and M. Muradoglu, Droplet formation in a flow focusing configuration: Effects of viscoelasticity, Phys. Fluids **28**, 123102 (2016).

[47] W. Du, T. Fu, Y. Duan, C. Zhu, Y. Ma, and H. Z. Li, Breakup dynamics for droplet formation in shear-thinning fluids in a flow-focusing device, Chem. Eng. Sci. **176**, 66 (2018).

[48] B. Steinhaus, A. Q. Shen, and R. Sureshkumar, Dynamics of viscoelastic fluid filaments in microfluidic devices, Phys. Fluids **19**, 073103 (2007).

[49] P. E. Arratia, L. A. Cramer, J. P. Gollub, and D. J. Durian, The effects of polymer molecular weight on filament thinning and drop breakup in microchannels, New J. Phys. **11**, 115006 (2009).

[50] Y. Ren, Z. Liu, and H. C. Shum, Breakup dynamics and dripping-to-jetting transition in a Newtonian/shear-thinning multiphase microsystem, Lab Chip **15**, 121 (2015).

[51] A. Gupta and M. Sbragaglia, Effects of viscoelasticity on droplet dynamics and break-up in microfluidic T-junctions: A lattice Boltzmann study, Eur. Phys. J. E **39**, 6 (2016).

[52] D. Qiu, L. Silva, A. L. Tonkovich, and R. Arora, Micro-droplet formation in non-Newtonian fluid in a microchannel, Microfluid. Nanofluid. **8**, 531 (2010).

[53] L. Sang, Y. Hong, and F. Wang, Investigation of viscosity effect on droplet formation in T-shaped microchannels by numerical and analytical methods, Microfluid. Nanofluid. **6**, 621 (2009).

[54] J. Husny and J. J. Cooper-White, The effect of elasticity on drop creation in T-shaped microchannels, J. Non-Newton. Fluid **137**, 121 (2006).

[55] V.-L. Wong, K. Loizou, P.-L. Lau, R. S. Graham, and B. N. Hewakandamby, Numerical studies of shear-thinning droplet formation in a microfluidic T-junction using two-phase level-set method, Chem. Eng. Sci. **174**, 157 (2017).

[56] V.-L. Wong, K. Loizou, P.-L. Lau, R. S. Graham, and B. N. Hewakandamby, Characterizing droplet breakup rates of shear-thinning dispersed phase in microreactors, Chem. Eng. Res. Des. **144**, 370 (2019).

[57] Y. Shi and G. H. Tang, Lattice Boltzmann simulation of droplet formation in non-Newtonian fluids, Commun. Comput. Phys. **17**, 1056 (2015).

[58] S. G. Sontti and A. Atta, CFD analysis of microfluidic droplet formation in non-Newtonian liquid, Chem. Eng. J. **330**, 245 (2017).

[59] T. Fu, L. Wei, C. Zhu, and Y. Ma, Flow patterns of liquid–liquid two-phase flow in non-Newtonian fluids in rectangular microchannels, Chem. Eng. Process. **91**, 114 (2015).

[60] E. Chiarello, L. Derzsi, M. Pierno, G. Mistura, and E. Piccin, Generation of oil droplets in a non-Newtonian liquid using a microfluidic T-junction, Micromachines **6**, 1825 (2015).

[61] E. Chiarello, A. Gupta, G. Mistura, M. Sbragaglia, and M. Pierno, Droplet breakup driven by shear thinning solutions in a microfluidic T-junction, Phys. Rev. Fluids **2**, 123602 (2017).

[62] R. B. Bird, R. C. Armstrong, and O. Hassager, *Dynamics of Polymeric Liquids* (Wiley, New York, 1987), Vol. 1.

[63] P. J. Carreau, Rheological equations from molecular network theories, Trans. Soc. Rheol. **16**, 99 (1972).

[64] D. Kehrwald, Lattice Boltzmann simulation of shear-thinning fluids, J. Stat. Phys. **121**, 223 (2005).

[65] Z. Guo, C. Zheng, and B. Shi, Discrete lattice effects on the forcing term in the lattice Boltzmann method, Phys. Rev. E **65**, 046308 (2002).

[66] S. Chen and G. D. Doolen, Lattice Boltzmann method for fluid flows, Annu. Rev. Fluid Mech. **30**, 329 (1998).

[67] D. d'Humières, Multiple-relaxation-time lattice Boltzmann models in three dimensions, Philos. Trans. R. Soc. A **360**, 437 (2002).

[68] P. Lallemand and L.-S. Luo, Theory of the lattice Boltzmann method: Dispersion, dissipation, isotropy, Galilean invariance, and stability, Phys. Rev. E **61**, 6546 (2000).

[69] T. Krüger, H. Kusumaatmaja, A. Kuzmin, O. Shardt, G. Silva, and E. M. Viggen, *The Lattice Boltzmann Method: Principles and Practice* (Springer, Cham, 2016).

[70] I. Ginzburg and D. d'Humières, Multireflection boundary conditions for lattice Boltzmann models, Phys. Rev. E **68**, 066614 (2003).

[71] Y. Q. Zu and S. He, Phase-field-based lattice Boltzmann model for incompressible binary fluid systems with density and viscosity contrasts, Phys. Rev. E **87**, 043301 (2013).

[72] A. M. Artoli and A. Sequeira, A. M. Artoli and A. Sequeira, Mesoscopic simulations of unsteady shear-thinning flows, in *Computational Science—ICCS 2006*, edited by V. N. Alexandrov, G. D. van Albada, P. M. A. Sloot, and J. Dongarra (Springer, Berlin, Heidelberg, 2006), pp. 78–85.

[73] T. Krüger, F. Varnik, and D. Raabe, Shear stress in lattice Boltzmann simulations, Phys. Rev. E **79**, 046704 (2009).

[74] A. K. Gunstensen, D. H. Rothman, S. Zaleski, and G. Zanetti, Lattice Boltzmann model of immiscible fluids, Phys. Rev. A **43**, 4320 (1991).

[75] X. Shan and H. Chen, Lattice Boltzmann model for simulating flows with multiple phases and components, Phys. Rev. E **47**, 1815 (1993).

[76] M. R. Swift, E. Orlandini, W. R. Osborn, and J. M. Yeomans, Lattice Boltzmann simulations of liquid-gas and binary fluid systems, Phys. Rev. E **54**, 5041 (1996).

[77] S. V. Lishchuk, C. M. Care, and I. Halliday, Lattice Boltzmann algorithm for surface tension with greatly reduced microcurrents, Phys. Rev. E **67**, 036701 (2003).

[78] A. Kuzmin, Z. L. Guo, and A. A. Mohamad, Simultaneous incorporation of mass and force terms in the multi-relaxation-time framework for lattice Boltzmann schemes, Philos. Trans. R. Soc. A **369**, 2219 (2011).

[79] M. Latva-Kokko and D. H. Rothman, Diffusion properties of gradient-based lattice Boltzmann models of immiscible fluids, Phys. Rev. E **71**, 056702 (2005).

[80] X. N. Shen and P. E. Arratia, Undulatory Swimming in Viscoelastic Fluids, Phys. Rev. Lett. **106**, 208101 (2011).

[81] S. Varagnolo, G. Mistura, M. Pierno, and M. Sbragaglia, Sliding droplets of xanthan solutions: A joint experimental and numerical study, Eur. Phys. J. E **38**, 126 (2015).

[82] D. A. Gagnon and P. E. Arratia, The cost of swimming in generalized Newtonian fluids: Experiments with *C. elegans*, J. Fluid Mech. **800**, 753 (2016).

[83] M. Hoorfar and A. W. Neumann, Recent progress in axisymmetric drop shape analysis (ADSA), Adv. Colloid Interfac. **121**, 25 (2006).

[84] J. D. Berry, M. J. Neeson, R. R. Dagastine, D. Y. C. Chan, and R. F. Tabor, Measurement of surface and interfacial tension using pendant drop tensiometry, J. Colloid Interface Sci. **454**, 226 (2015).

[85] M. J. Fuerstman, A. Lai, M. E. Thurlow, S. S. Shevkoplyas, H. A. Stone, and G. M. Whitesides, The pressure drop along rectangular microchannels containing bubbles, Lab Chip **7**, 1479 (2007).